

Abundance analysis for long-period variables

II. RGB and AGB stars in the globular cluster 47 Tuc

T. Lebzelter¹, W. Nowotny¹, K.H. Hinkle², S. Höfner³, and B. Aringer³

¹ University of Vienna, Department of Astrophysics, Türkenschanzstrasse 17, A-1180 Vienna, Austria
e-mail: thomas.lebzelter@univie.ac.at

² National Optical Astronomy Observatory, 950 N.Cherry Avenue, Tucson, Arizona 85726, USA

³ Departement for Physics and Astronomy, Division of Astronomy and Space Physics, Uppsala University, Box 516, 75120 Uppsala, Sweden

Received ; accepted

ABSTRACT

Context. Asymptotic giant branch (AGB) stars play a key role in the enrichment of galaxies with heavy elements. Due to their large amplitude variability, the measurement of elemental abundances is a highly challenging task that has not been solved in a satisfactory way yet.

Aims. Following our previous work we use hydrostatic and dynamical model atmospheres to simulate observed high-resolution near-infrared spectra of 12 variable and non-variable red giants in the globular cluster 47 Tuc. The 47 Tuc red giants are independently well-characterized in important parameters (mass, metallicity, luminosity). The principal aim was to compare synthetic spectra based on the dynamical models with observational spectra of 47 Tuc variables. Assuming that the abundances are unchanged on the upper giant branch in these low-mass stars, our goal is to estimate the impact of atmospheric dynamics on the abundance determination.

Methods. To estimate abundances, we measured the equivalent widths of selected features in observed spectra and compared the results with predictions from a set of hydrostatic and dynamical model atmospheres resembling 47 Tuc AGB stars in their fundamental parameters. Our study includes lines of ^{12}CO , ^{13}CO , OH, and Na. Furthermore, we investigated the variations in line intensities over a pulsation cycle.

Results. We present new measurements of the C/O and $^{12}\text{C}/^{13}\text{C}$ ratio for 5 non-variable red giants in 47 Tuc. The equivalent widths measured for our 7 variable stars strongly differ from the non-variable stars and cannot be reproduced by either hydrostatic or dynamical model atmospheres. Nevertheless, the dynamical models fit the observed spectra of long-period variables much better than any hydrostatic model. For some spectral features, the variations in the line intensities predicted by dynamical models over a pulsation cycle give similar values as a sequence of hydrostatic models with varying temperature and constant surface gravity.

Conclusions. Our study of the dynamical effects on abundance determination visible in these well-characterized cluster stars prepares the ground for the long-term goal of deriving abundances for variable AGB stars in general.

Key words. stars: late-type – stars: AGB and post-AGB – stars: atmospheres – stars: abundances – line-profiles

1. Introduction

The evolution of low- and intermediate-mass stars along the red giant branch (RGB) and the asymptotic giant branch (AGB) is accompanied by major mixing events that change the elemental abundance pattern derivable for the stellar atmosphere. The surface abundances then allow a view into the nucleosynthesis processes in the stellar interior and provide important clues to the origin of the elements in the interstellar medium and ultimately in ourselves. The main tool for studying the abundance pattern is high-resolution spectroscopy. However, deducing the element abundances from the spectra requires an understanding of the physical conditions in the line-forming atmospheric layers. Two properties of red giants, in particular of those on the AGB, complicate this procedure: very extended atmospheres and dynamical effects due to radial pulsation. Several authors have worked on this question in the past, in particular, Scholz (1992), Bessell et al. (1996), and McSaveney et al. (2007).

In the first paper of this series (Lebzelter et al. 2010, Paper I), we summarised the previous studies and presented a new investigation of the dynamical effects on stellar abundance de-

terminations based on the dynamical model atmospheres by Höfner et al. (2003). The observed changes in line depth over a pulsation cycle cannot be reproduced by a simple sequence of hydrostatic models of varying effective temperature or surface gravity, because the pulsation leads to a clearly non-hydrostatic atmospheric structure (e.g. Nowotny et al. 2010) producing very different line depths. The well known phenomenon of line doubling (e.g. Hinkle et al. 1982) adds further complication to this matter. The changes in line strength over a light cycle produce a loop in an equivalent width (EW) vs. $(J - K)$ diagram; i.e., the rising and descending branch of the light curve do not show the same line strength at the same near-infrared (NIR) colours. This result is also found qualitatively in the observational data of one field mira analysed in Paper I.

The conclusion from Paper I is that only a dynamical model atmosphere can properly describe the atmospheric structure and temporal change in highly variable stars at the tip of the giant branch. Therefore, it is timely to ask if state-of-the-art dynamical models can be used to derive abundances for such stars. The goal of the current paper is to explore this question by comparing independently well-characterized objects with dynamical

model atmospheres for which the fundamental parameters (M , L , $[\text{Fe}/\text{H}]$, pulsation period, and T_{eff}) were chosen to fit the observed targets.

Cluster stars are an excellent testbed for such investigations. Parameters, such as mass, metallicity, and luminosity, can be determined on the basis of a large number of stars, without relying on the giants. This is a major advantage since deriving abundances for cool giants is a problem with many degrees of freedom so that any constraints of parameters from independent sources reduce the uncertainties significantly.

The study of changes in the intensity and profile of an atomic or molecular line in cool giants is hampered by the large number of blending spectral features. To minimize the impact of line blending, our strategy – previously presented in Paper I – is to study NIR lines in metal-poor objects. With plenty of atomic and several series of molecular lines available, the NIR is the preferred wavelength range to derive element abundances in cool giants. In the present paper, we continue this strategy.

We decided to use NIR spectra of 47 Tuc red giants for our study since they combine the advantages of (i) cluster membership and (ii) reduced line blending. We constrain the abundances of the variable stars in advance by deriving selected element abundances for a sample of non-variable stars in that cluster with the help of hydrostatic model atmospheres.

2. The 47 Tuc reference sample

2.1. Observations

47 Tuc is one of the closest globular clusters. It has a well populated giant branch, and the AGB stars of that cluster have been studied in several papers of our group (see Lebzelter et al. 2005, 2006). There we reviewed the cluster's main parameters as found in the literature. For the present study we use a distance modulus ($m - M$) of 13.5 mag. Interstellar extinction and reddening is low towards this cluster, we took a value of $E(B - V) = 0.024$ and $R_V = 3.1$ as in Lebzelter et al. (2005). We use a metallicity $[\text{Fe}/\text{H}] = -0.7$. For modelling stars on the upper giant branch of 47 Tuc, we set the current mass to $0.6 M_{\odot}$ following Lebzelter & Wood (2005).

From the 42 known variable red giants in 47 Tuc (Lebzelter & Wood 2005, see their Table 1), we selected a subset of seven targets for our abundance study. The main characteristics of these long period variables (LPVs; object identifications V followed by a number) are listed in Table 1. Table 1 also contains the corresponding data for our sample of non-variable RGB stars in 47 Tuc (object identifications Lee followed by a number; identified originally by Lee 1977). Two different data sets of observational spectroscopy were used in this work.

First, we obtained single-epoch high-resolution ($R = 50\,000$) NIR spectra for the complete sample of stars using the Phoenix spectrograph at Gemini South (Hinkle et al. 2003). Observations were done on three consecutive nights in December 2002 using two wavelength settings around 1.555 and $2.341 \mu\text{m}$ (cf. Fig. 4). Each setting covers a spectral range of approximately 100 \AA . These single-epoch spectra were used to derive general abundance information in Sect. 4.1.

Second, we analysed a spectroscopic time series around $1.630 \mu\text{m}$ ($R = 37\,000$; cf. Fig. 6) for a subsample of objects (V1, V2, V3, V4, V11, and V18), obtained at Mount Stromlo Observatory in 2002. These spectra were previously used in a study of the velocity variations of the 47 Tuc LPVs (Lebzelter et al. 2005), and we refer to that publication for further details on the observations. The Mount Stromlo observations included all the

variables from the Gemini sample but not the RGB stars. These time series of spectra were used to gather information on the temporal variability of EWs in Sect. 4.2.

The observed spectra were reduced using standard techniques for NIR spectra. Wavelength calibration was done with spectra of K-type standard stars. The wavelength regions were selected to include only a negligible (H -band) or low (K -band) contamination by telluric lines which were removed. The spectra were corrected for radial velocity shifts (stellar motion, atmospheric kinematics) so that the line centres are at the laboratory wavelengths. For line identification we used the NIR spectral atlas of Arcturus provided by Hinkle et al. (1995). Instrumental distortion of the (pseudo)continuum was removed. For the Mount Stromlo data we had a few cases where two spectra of the same star were obtained on consecutive nights. These spectra were not combined but analysed separately and used for constraining the measurement uncertainty.

2.2. Stellar parameters

The membership of our stellar sample in a globular cluster makes determining some stellar parameters (e.g. L , M , $[\text{Fe}/\text{H}]$) simpler and more reliable than for field stars. A notable exception, however, is the effective temperature that we estimate from NIR photometry. We did not obtain simultaneous NIR photometry. For the Lee stars we used $(J - K)$ values from Frogel et al. (1981). For the small-amplitude variables V7, V11, and V18, we used the values given in Lebzelter & Wood (2005). For the large amplitude variables, V1, V2, V3, and V4, which show a significant brightness amplitude also in the NIR, we first derived the pulsation phase at the time of the observation using light curve data presented in Lebzelter & Wood (2005). Based on the photometric variability range in the NIR of our sample stars, compiled from various individual measurements and short time series available in the literature (Glass & Feast 1973; Frogel et al. 1981; Frogel 1983; Menzies & Whitelock 1985; Frogel & Elias 1988; Lebzelter et al. 2005), we estimated infrared colours for the calculated pulsation phase at the time of the Gemini observations. These are the values given in Table 1. For the large-amplitude variables, we were able to determine the colour change with good coverage of the whole light cycle (e.g. Menzies & Whitelock 1985). However, even in those cases the total range in $(J - K)$ for any star does not exceed $0^{\text{m}}.15$, so that a large error in our $(J - K)$ values can be excluded. Phasing of the Mount Stromlo measurements was done using the parallel light curves given in Lebzelter et al. (2005) and Lebzelter & Wood (2005). All photometry was transformed to the photometric system of Bessell & Brett (1988) that was also used for calculating our synthetic photometry.

For relating NIR colour and T_{eff} , we used hydrostatic models as outlined in detail in Sect. 3.2. With the distance and turn-off mass of 47 Tuc, we can estimate the typical L , T_{eff} , and $\log g$ values for our cluster stars. Non-variable stars are found in the temperature range between 3800 and 4200 K, and their surface gravity $\log g$ is between 0.6 and 1.0. For the variable stars we get temperatures between 3500 and 3750 K and $\log g$ values between -0.2 and 0.5 . However, these estimates assume a hydrostatic structure and therefore have to be taken with some caution. The calculated stellar parameters for each star are given in the final three columns of Table 1. Our temperatures are in good agreement with the values derived by Lebzelter & Wood (2005), but are somewhat higher than the earlier values given in Feast (1996). Also listed in Table 1 are estimates for the luminosity L_{\star} at the phase of observation given there.

Table 1. Properties of the 47 Tuc stars (LPVs, non-variable RGB stars), all of which are assumed to have $M_\star = 0.6 M_\odot$ and $[\text{Fe}/\text{H}] = -0.7$ dex (Paper I). The photometric data is described in Sect. 2. K and $(J - K)$ are given for the corresponding pulsation phase ϕ . Periods are taken from Lebzelter & Wood (2005) (uncertain values are marked with a colon). The photometric variations ΔV were adopted from Lebzelter et al. (2005), while the estimates for T_{eff} and $\log g$ are described in Sect. 3.2.

Object-ID	K [mag]	$(J - K)_0$ [mag]	Period [d]	Pulsation phase ϕ	ΔV [mag]	L_\star [L_\odot]	T_{eff} [K]	$\log g$ [cm s^{-2}]
V1	6.20	1.24	221	0.90	4.8	4760	3410	-0.2
V2	6.28	1.14	203	0.35	4.5	4470	3620	-0.1
V3	6.26	1.18	192	0.18	3.5	4590	3540	-0.1
V4	6.68	1.19	165	0.80	2.5	3260	3520	0.1
V7	6.96	1.16	52	–	0.4	2450	3590	0.2
V11	6.70	1.15	160:	–	0.2	3110	3600	0.1
V18	7.46	1.07	83:	–	0.25	1550	3750	0.5
Lee 1505	8.53	0.96	–	–	–	710	4020	0.9
Lee 1510	8.77	0.91	–	–	–	610	4090	1.0
Lee 1603	7.95	1.07	–	–	–	1150	3800	0.6
Lee 2426	8.50	0.96	–	–	–	720	4020	0.9
Lee 4603	8.75	0.88	–	–	–	630	4170	1.0

Mass loss is a critical question when comparing models of AGB stars with observations. However, measurement of mass loss rates remains a very challenging task. Several studies have dealt with the mass loss from the 47 Tuc AGB variables. For our sample, the occurrence of dusty mass loss in V1 to V4 and in V18 is confirmed both by an infrared excess (e.g. Ramdani & Jorissen 2001; McDonald et al. 2011) and by mid-infrared spectroscopy (Lebzelter et al. 2006). V7 seems to be dust free (Lebzelter et al. 2006). Estimates of mass loss rates found in the literature cluster around 10^{-6} to $10^{-5} M_\odot \text{yr}^{-1}$ for the stars on the upper AGB of this cluster (Frogel & Elias 1988; Origlia et al. 1997; McDonald & van Loon 2007).

In Fig. 1 we show the location of our sample stars in a colour-magnitude diagram (CMD) of the cluster. The CMD was compiled from 2MASS data within 4 arc minutes of the approximate cluster centre. The 2MASS data were dereddened and transferred to the Bessell system. The brightness of the RGB tip is marked according to Lebzelter & Wood (2005), the location of the horizontal branch and the RGB bump are consistent with the findings of Salaris et al. (2007). All our variables are located on the uppermost part of the giant branch, and with the exception of V18, they are all above the RGB tip, i.e. they are AGB stars. The non-variable stars in our sample are either on the early AGB or on the RGB.

3. Methods

We use the same approach as in Paper I to characterize both the observed spectra of 47 Tuc stars and the synthetic ones computed for hydrostatic and dynamical atmospheric structures, namely the measurement of EWs, of selected atomic and molecular lines, and of molecular band heads. The spectroscopic features were selected to determine various aspects of the abundance pattern in the 47 Tuc stars, namely (i) the C/O ratio, (ii) the isotopic ratio of carbon $^{12}\text{C}/^{13}\text{C}$, (iii) the ratio of two transitions of the same species with different excitation of the ground level (radial atmospheric structure), and (iv) the abundance of an atomic species (Na). For the study of (v) the feature variability over a pulsation cycle, we selected the CO 4-1 P27 line, which is the least blended line within the spectral range covered by the Mount Stromlo observations.

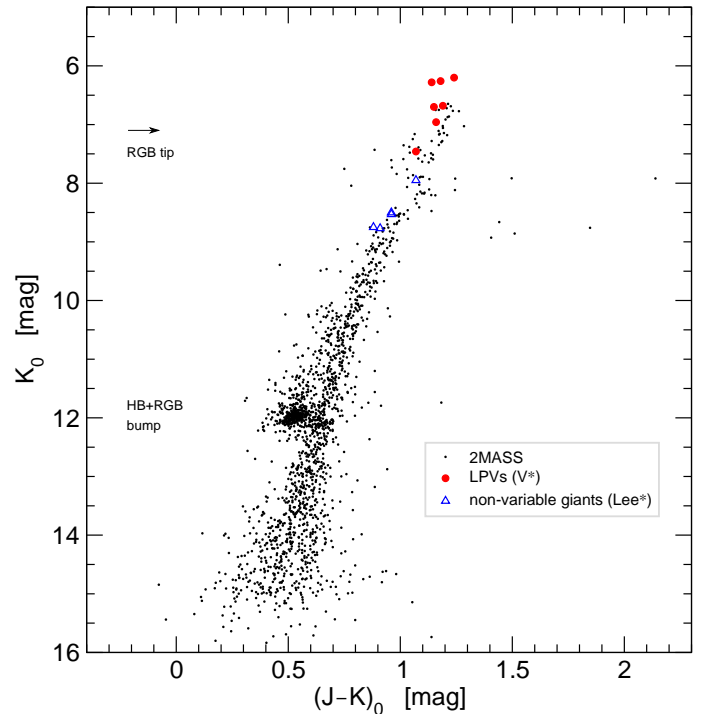


Fig. 1. Colour-magnitude diagram of 47 Tuc based on 2MASS data. The location of our sample stars are shown, divided into variable stars (red filled circles) and non-variable stars (blue open triangles). The photometry has been transferred to the Bessell system.

Standard methods within IRAF were used to measure EWs. For selecting the appropriate measurement range around each line centre, we considered the maximum feature width observed in any of the analysed hydrostatic spectra (see also Sect. 3.3). In the case of the measured band heads, the short wavelength limit was set to the cut-off wavelength while the long-wavelength limit was set at an arbitrary position within the band head. All spectra were analysed with the same set of measurement limits for the studied spectral features as listed in Table 2. Since we had shifted the spectra so that the line cores always fall on the same position in wavelength (averaged over the observed spec-

Table 2. List of the features studied. Columns 3 and 4 give the borders of the spectral ranges applied to determine equivalent widths (cf. Paper I).

Species	Transition	λ_{start}	λ_{end}	Note
OH	blend	15568.6 Å	15572.1 Å	1
OH	2-0 P _{1e} 11.5	15572.1 Å	15574.8 Å	1
OH	2-0 P _{1f} 11.5	15574.9 Å	15578.6 Å	1
¹² CO	3-0 band head	15581.1 Å	15585.7 Å	1, 2
¹² CO	4-1 P27	16307.1 Å	16309.1 Å	5
Na		23383.6 Å	23387.4 Å	4
¹² CO	3-1 R18	23438.5 Å	23443.1 Å	3
¹² CO	3-1 R82	23443.1 Å	23445.6 Å	3
¹³ CO	2-0 band head	23447.1 Å	23452.3 Å	2

Notes. The last column denotes the purpose of the individual features using the following designations: 1 → C/O ratio; 2 → ¹²C/¹³C; 3 → atmospheric structure; 4 → [Na/Fe]; 5 → temporal variation.

tral range), the measurement range could be kept constant and independent of pulsation phase.

3.1. Model atmospheres and spectral synthesis

Two different types of atmospheric models were used to calculate synthetic spectra and photometry in this work, the parameters of which were chosen to resemble the various 47 Tuc objects introduced in Sect. 2 and Table 1. First, we produced a grid of hydrostatic, dust-free COMARCS model atmospheres (O-rich). Being representative of the non-variable RGB stars in 47 Tuc, these models also serve as the hydrostatic reference grid for the subsequent illustration of dynamic effects. The models were computed for the parameter range specified in Table 3 as described in detail in Aringer et al. (2009).

Second, we used a small grid of O-rich dynamic model atmospheres to investigate the effects of pulsation and mass loss on the resulting spectra. The aim was to produce models resembling the LPVs in 47 Tuc. The models combine time-dependent dynamics with frequency-dependent radiative transfer, allowing us to take pulsation-induced shock waves and opacities from atoms, molecules, and dust grains into account. Stellar pulsation is simulated by varying the gas velocity and the luminosity at the inner boundary that is located below the stellar photosphere. The basic physical equations, assumptions, and methods used for computing these models are described in Höfner et al. (2003), but some adjustments were made compared to these earlier models to accommodate the properties of the present stellar sample, in particular regarding the driving mechanism of the stellar wind.

As discussed in Sect. 2, observations indicate both ongoing mass loss and the presence of dust in the outflows of the 47 Tuc LPVs. However, it is still a matter of debate as to what drives the winds of O-rich AGB stars, in particular at low metallicity and relatively high effective temperature, as in this sample. Therefore, we used a parameterized description of the driving force of the wind, suitable for mimicking radiation pressure on different dust species or other wind mechanisms. More specifically, the current approach is based on a parameterized treatment of dust formation and grain opacities as described in Bladh & Höfner (2012). Given the uncertainties regarding the driving mechanism and relevant dust species, we computed models with two types of forces: (i) radiation pressure due to true absorption by dust grains (which also has significant effects on the resulting spectral

Table 3. Parameter ranges covered by the applied grid of hydrostatic (COMARCS) model atmospheres. Similar to the approach followed in Paper I, we kept the other parameters constant for all the models: $M_{\star} = 1 M_{\odot}$, [Fe/H] = −0.7 dex, $\xi = 2.5 \text{ km s}^{-1}$.

	Range:	Stepwidth:
C/O	0.48 / 0.25	
T_{eff} [K]	2600 ... 4500	$\Delta=100$
$\log(g \text{ [cm/s}^2\text{]})$	0.0 ... +2.5	$\Delta=0.5$

Notes. The isotopic ratio ¹²C/¹³C was varied only for the spectral synthesis.

energy distribution), and (ii) an acceleration due to pure scattering on dust grains (or another force, with a similar radial profile), not causing significant circumstellar reddening. In terms of the formulae given in Bladh & Höfner (2012, their Sect. 3.2), these two cases correspond to $f_{\text{abs}} = 1$ and $f_{\text{abs}} = 0$, respectively, where f_{abs} defines the fraction of the dust opacity that is to be considered as true dust absorption. For the other parameters we assume $\kappa_0 = 3 \text{ cm}^2/\text{g}$ (scaling factor of the overall absorption), $p = 0$ (i.e. no dependence on wavelength) and a condensation temperature $T_c = 1500 \text{ K}$.

Extending the set of two models presented in Paper I, we varied the stellar parameters of the grid models (cf. Table 4) to represent a characteristic 47 Tuc mira, for instance V3 (upper row of the 2×2-table), or an LPV in this system with less pronounced variations such as LW12 (lower row). In addition, we chose two different values for the C/O ratio, namely 0.48 (solar) and 0.25, as labelled in the main columns of Table 4. For each combination of these fundamental parameters we computed dynamical models with different pulsation properties, parameterized by the period, the piston velocity amplitude Δu_p , and the luminosity amplitude parameter f_L (see Nowotny et al. 2010 for a definition, and Eriksson et al. 2014 for a discussion). This resulted in models for pulsating atmospheres (P), as well as models that, in addition, develop a wind (PM).

The radial atmospheric structures (temperature-pressure) of the hydrostatic and dynamic model atmospheres were used to calculate synthetic spectra under the assumptions of chemical equilibrium, as well as conditions of LTE following the approach of Aringer et al. (2009). We adopted the values for solar composition provided by Anders & Grevesse (1989), except for C, N, and O, which were taken from Grevesse & Sauval (1994). For more details on our calculation of synthetic spectra and photometry, we refer to the extensive description in Paper I.

3.2. Evaluation of the models

In Fig. 2 we illustrate the relation of $(J - K)$ and T_{eff} as derived from our hydrostatic model atmospheres for two different values of surface gravity. The shaded area indicates the $(J - K)$ range of the 47 Tuc giants studied in this paper (see Sect. 2). We note that there is a turnaround of the relations in the range 3200 to 3400 K resulting in bluer colours for cooler stars. This result of the modelling has been seen already in Paper I. The figure shows a semi-empirical relation derived by Worthey & Lee (2011), which does not show this behaviour. We suspect that this difference is due to the lack of dust in our hydrostatic models.

Table 4. Characteristics of the nine dynamic model atmospheres used for the spectral synthesis listed in a 2×2 table for two different sets of stellar parameters (given in the leftmost column) and two different C/O ratios (given in the top row). The following parameters are coded in the names of the models (e.g. L4C048AP): luminosity (L4), C/O ratio (0.48), the combination of the piston-velocity amplitude Δu_p and the luminosity-amplitude parameter f_L (A), as well as a simplified mass-loss information (P = only pulsating, PM = pulsating and mass-losing).

		C/O = 0.48			C/O = 0.25		
	Model:	L4C048AP	L4C048CPM	Model:	L4C025AP	L4C025CPM1	L4C025CPM2
$L_\star = 4000 L_\odot$	Δu_p [km s ⁻¹]	2	4	Δu_p [km s ⁻¹]	2	4	4
$M_\star = 0.6 M_\odot$	f_L	4	3	f_L	4	3	3
$T_\star = 3500$ K	Δm_{bol} [mag]	0.86	1.35	Δm_{bol} [mag]	0.86	1.35	1.35
[Fe/H] = −0.7 dex	κ_0 [cm ² g ⁻¹]	0	3	κ_0 [cm ² g ⁻¹]	0	3	3
$\log g = -0.26$	f_{abs}	–	1	f_{abs}	–	1	0
$P = 200$ d	$\langle \dot{M} \rangle$ [M_\odot yr ⁻¹]	–	2.0×10^{-7}	$\langle \dot{M} \rangle$ [M_\odot yr ⁻¹]	–	1.5×10^{-7}	5.0×10^{-7}
	$\langle u \rangle$ [km s ⁻¹]	–	13.0	$\langle u \rangle$ [km s ⁻¹]	–	13.8	14.5
	Model:	L3C048AP	L3C048BP	Model:	L3C025AP	L3C025BP	
$L_\star = 3000 L_\odot$	Δu_p [km s ⁻¹]	2	3	Δu_p [km s ⁻¹]	2	3	
$M_\star = 0.6 M_\odot$	f_L	4	4	f_L	4	4	
$T_\star = 3550$ K	Δm_{bol} [mag]	0.59	0.91	Δm_{bol} [mag]	0.59	0.91	
[Fe/H] = −0.7 dex	κ_0 [cm ² g ⁻¹]	0	3	κ_0 [cm ² g ⁻¹]	0	3	
$\log g = -0.11$	f_{abs}	–	0	f_{abs}	–	0	
$P = 120$ d	$\langle \dot{M} \rangle$ [M_\odot yr ⁻¹]	–	–	$\langle \dot{M} \rangle$ [M_\odot yr ⁻¹]	–	–	
	$\langle u \rangle$ [km s ⁻¹]	–	–	$\langle u \rangle$ [km s ⁻¹]	–	–	

Notes. Notation adopted from previous works (Lebzelter et al. 2010; Nowotny et al. 2010, 2013). First column: parameters of the hydrostatic initial model (luminosity L_\star , mass M_\star , effective temperature T_\star , metallicity [Fe/H]) together with the pulsation period P of the piston at the inner boundary. Δu_p , f_L : velocity amplitude and luminosity-amplitude parameter of the inner boundary condition (piston) used to simulate the pulsating stellar interiors; Δm_{bol} : resulting bolometric amplitude; κ_0 : total dust opacity; f_{abs} : fraction assumed to be true absorption (see Sect. 3.1); $\langle \dot{M} \rangle$: mean mass-loss rate; $\langle u \rangle$: mean outflow velocity at the outer boundary.

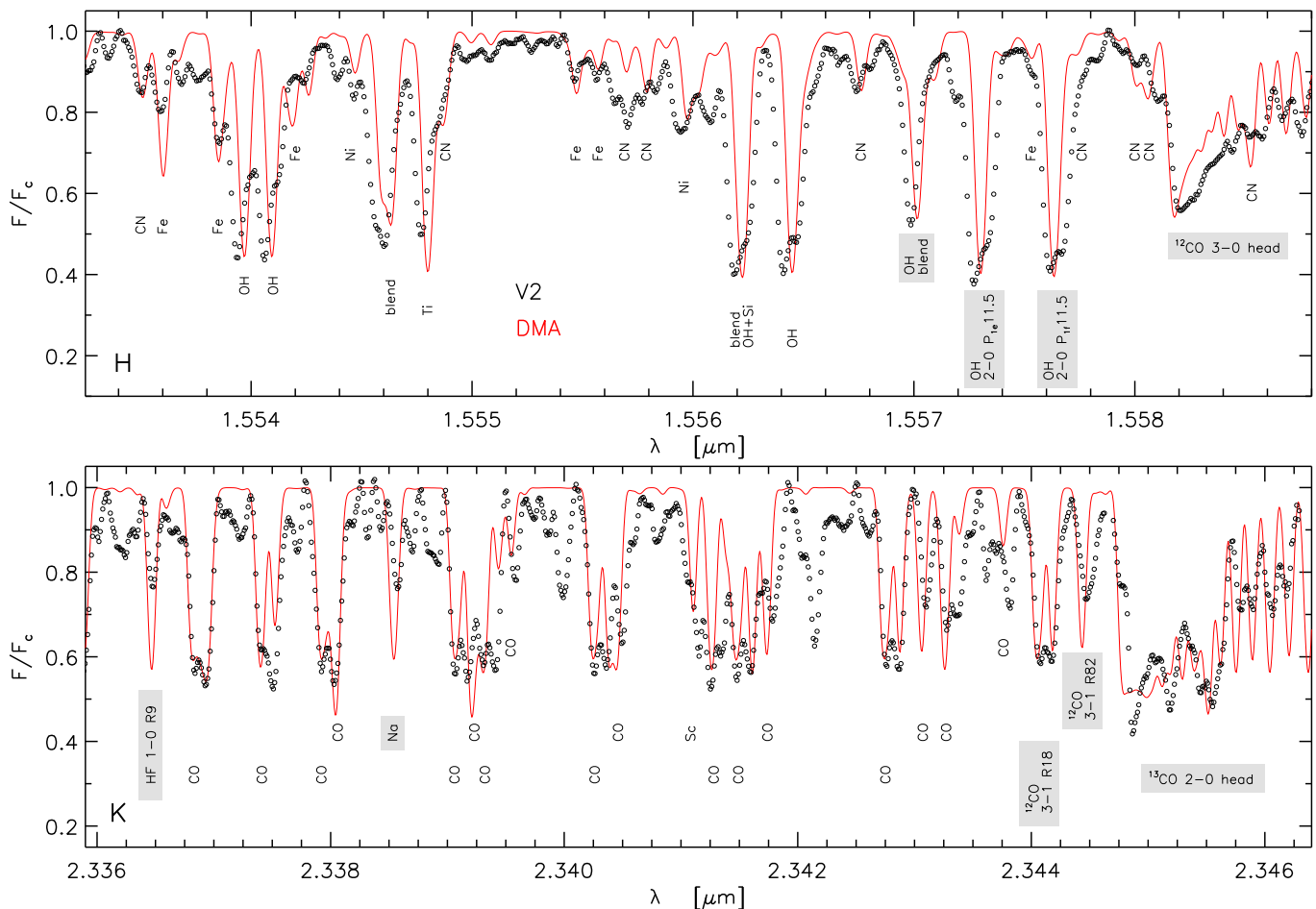


Fig. 5. Same as Fig. 4 but for one of the 47 Tuc variable stars, namely V2, compared with the best-fitting dynamical model L3C025BP at pulsation phase $\phi = 0.8$.

tent with the results of Bladh et al. (2013), indicating again that the circumstellar envelopes of O-rich AGB stars are rather transparent at NIR wavelengths, which makes radiation pressure by true absorption on dust grains an unlikely driving mechanism for these stars.¹ For illustrative purposes, we decided to keep L4C025CPM1 in our analysis keeping in mind its limitations in terms of the description of dust and its non-fitting NIR colours.

We also calculated photometric amplitudes from our models. In the K -band, L4C025AP, L3C025AP, and L3C025BP all show a similar amplitude of 0.4–0.5 magnitudes. L4C025CPM1 produces a K amplitude of 0.9. V amplitudes of the 47 Tuc variables can be found in Lebzelter & Wood (2005), Table 2. The K amplitude is approximately 20% of the visual amplitude (see Lebzelter & Wood 2005). Therefore, we expect total K amplitudes around 0.6 to 0.9 magnitude for V1 to V3 and 0.4 magnitudes for V4. The calculated light amplitudes from our models are thus in reasonable agreement with the observed values, but only the L4C025CPM1 model produces enough amplitude to model the light amplitude of the brightest stars in our sample, probably due to variations in the dust absorption. However, as

we saw in Fig. 3, this model results in an unrealistic variation in $(J - K)$.

3.2.2. Analysis of the high-resolution spectra

As a next step, we compared the observed and synthetic spectra for the non-variable case (see Fig. 4 for an illustrative example). The best-fitting hydrostatic model was chosen on the basis of the $(J - K)$ colour and the line strengths of the spectral features listed in Table 2 and also marked in Fig. 4. For most spectral lines, both in the H - and in the K -band region, the agreement between observed and synthetic spectra is very good. In the H -band the largest difference is found for the observed feature at the location of the Ni line at $1.5544\mu\text{m}$. Quite obviously there is a blending feature that has not been identified yet. Since it is quite broad, we suspect that it is either a mix of several blending atomic lines or a structure resulting from a molecular species. Besides that, we see minor differences in some of the CN lines. This could indicate either that the low N abundance is too low in our models or that there is inadequate line data. In the K -band, no particular differences between observed and modelled spectra were found except for a difference in the strengths of the HF line. This is very likely due to an incorrect F abundance in our models. The F abundance of 47 Tuc stars will be discussed in a forthcoming paper (Hren et al., in preparation). In any case,

¹ For solar metallicity, scattering of photons on Fe-free silicate grains seems to be a viable alternative as demonstrated by Höfner (2008) and Bladh et al. (2013). At the low metallicity and rather high effective temperatures of the 47 Tuc stars, however, this option is also unlikely, leaving the question about the driving mechanism open at present.

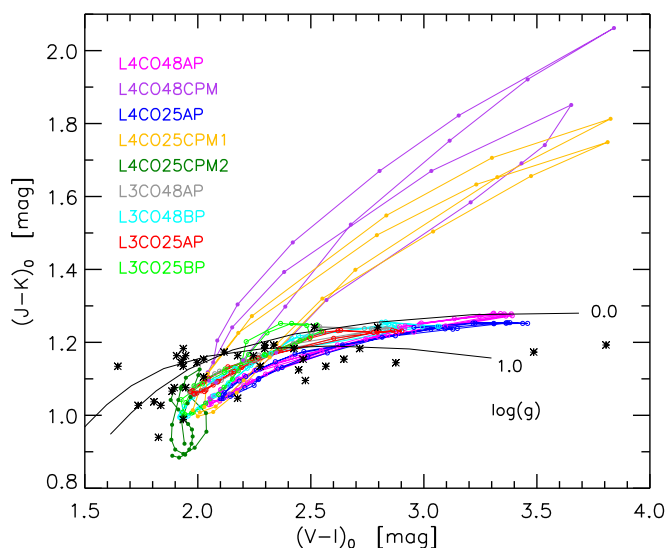


Fig. 3. Colour-colour diagram for the 47 Tuc variables from Lebzelter & Wood (2005), marked with asterisks. Overplotted are temperature sequences of hydrostatic MARCS models for two different values of $\log g$ (black solid lines), and the phase-dependent photometry for the dynamical model atmospheres.

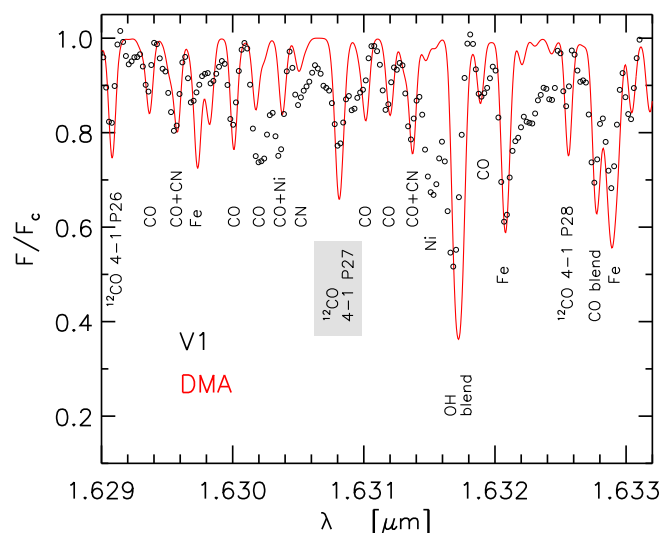


Fig. 6. Comparison of one observed spectrum of the 47 Tuc variable V1, compared with the corresponding synthetic spectrum of model L4CO25AP at minimum light during the light cycle (phase $\phi = 0.5$). This additional wavelength range contains the ^{12}CO 4–1 P27 line, which was used for investigating the EW variability in Sect. 4.2.

none of the deviations seen in the H -band has any effect on the line strengths measurements in our study.

In Fig. 5 we give an illustrative example for a comparison between a variable star (V2) and a dynamical model. This spectrum was selected because it shows the line doubling that Lebzelter et al. (2005) previously observed in V1, V2, and V3. In this case, the model and the specific phase for comparison was selected by eye, with the aim of reproducing the mentioned line doubling at least in the K -band. However, V2 is in its post-maximum phase, while the model plotted in Fig. 5 is pre-maximum. The measured EWs of the ^{12}CO and ^{13}CO bandheads differ by 0.2 and 0.1 Å, respectively. The observed $(J - K)$ value

is approximately 0.04 mag lower than the corresponding model value. Still the dynamical model fits the observation significantly better than any of our hydrostatic models.

At this point, we excluded another model from our analysis, namely L4CO25CPM2. Although photometry derived from the model is in good agreement with the colour range of the 47 Tuc stars (Fig. 3), the model spectra show strong emission lines over most of the pulsation cycle. The emission lines are not visible in any of the observed spectra and prohibit a meaningful measurement of line strengths within our analysis scheme.

3.3. Uncertainties of the EW measurements

In the case of the EWs measured in the spectra of the 47 Tuc stars we note three possible sources of uncertainty: the observational noise, the location of the continuum level, and the effect of variations in blending features and differential velocity fields in the stellar atmosphere. For the Gemini data, the S/N of the spectra of the cluster stars (both variables and non-variable stars) was between 150 and 250 except for the H band spectrum of V18, which had a S/N of 120. Due to the high quality of the spectra and the low contamination by telluric lines, the influence of the observational noise only plays a minor role in the error budget. This is a bit different for the Mount Stromlo time series spectra that have a S/N around 50.

Defining a continuum level is quite a challenging task, in particular for the coolest objects in our sample owing to not having enough continuum points. In setting the level of the pseudo-continuum, we followed the strategy described in Paper I. Observed and synthetic spectra were handled the same way; i.e., we measured line strengths in the synthetic spectra relative to a local pseudo continuum and not the true continuum level to allow for a comparison with the observations. We did some experiments by changing the continuum level within an acceptable range among the highest points in the spectra to estimate the error and found maximum values of ± 0.02 Å in EW for individual lines and about ± 0.04 Å for the band heads studied.

Even at high spectral resolution in the NIR, the analysis of a spectral line without any blending from neighbouring features is almost impossible. Again, the problem is more pronounced for the cool variables at the tip of the giant branch. This confusion is unavoidable, but since the effect is expected to be the same in the observed and synthetic spectra, it should not be a major problem for our analysis. A more significant challenge is the variability of the line profiles within a pulsation cycle. Problems here are twofold. First, the line centre moves in wavelength according to the variable atmospheric velocity field. As in Paper I we handle this problem by shifting the spectra to laboratory wavelength. A difficulty that arises for V1, V2, and V3 at some phases is that the velocity shift is not necessarily the same for all atomic or molecular transitions. This was taken into account when positioning the lower and upper limits for measuring the EWs. The second problem in this context are the changes in the line width once secondary components appear. All the limits for measuring the EW were set to the maximum width possible without including the next feature of high or moderate strengths. This selection was done on the basis of the hydrostatic model spectra. However, in a few cases this width was not sufficient to include all additional line components that emerge due to the velocity field in the photosphere. An estimate of the size of this uncertainty is not possible.

For the Mount Stromlo spectra, we occasionally have spectra of the same star taken on two consecutive nights. Assuming that

the spectral variations on that time scale will be negligible, we used a direct comparison of these two spectra for estimating the uncertainty of our measured equivalent width. We consistently found uncertainties of $\pm 0.03 \text{ \AA}$ for the results from this data set.

4. Results

4.1. Comparing models with single-epoch observations

The goals of our analysis are twofold. One is to investigate the spectroscopic differences between hydrostatic and dynamical models based on a larger grid of models than in Paper I. As outlined there, we find some basic characteristics of the spectral changes with pulsation phase, in particular the loop of line EW against $(J-K)$. The loops in line strength versus colour show that the line-forming region has a different structure on the rising and the descending branches. We could confirm this effect with our extended set of dynamical model atmospheres. The second goal is to compare the modelling results with observational data to estimate several basic stellar parameters for our sample of evolved red giants in 47 Tuc. In the following, both goals will be pursued in parallel. We use a fixed value for the metallicity of the 47 Tuc stars based on the considerable number of measurements of this quantity available in the literature, and we explore the sensitivity of the chosen spectral features to fundamental stellar parameters.

4.1.1. Constraining the C/O ratios

In Fig. 7 we use two prominent features in the H -band spectrum, namely an OH line and the ^{12}CO 3-0 band head, to study the dependence of the measured equivalent widths on the C/O ratio. Plotting two feature strengths against each other instead of plotting feature strength against $(J-K)$ has the advantage of better separating the effects of temperature T_{eff} and $\log g$. In this and all the following plots, the full temperature range, 2600 to 4500 K, is shown for the hydrostatic models. For the dynamical models, we typically plot two consecutive light cycles.

For determining the C/O ratio we assume a scaled solar abundance of oxygen. Since oxygen may be over- or under-abundant in the cluster stars relative to the scaled solar value, our measurement of the CO band head strengths nominally measures only C^*O . To explore this effect, we did some test calculations by changing the oxygen abundance by $+0.2$ dex. The CO-band-head strength depends on C/O, T_{eff} , $\log g$, and the oxygen abundance. Increasing either C/O or O/H leads in both cases to an increase in the feature strengths. The OH lines, in particular the OH blend near $1.557 \mu\text{m}$, are sensitive to the same parameters². However, the dependency on C/O is going the opposite way; i.e., the lines are getting weaker for a higher C/O ratio. Using T_{eff} and $\log g$ values from Table 1, we can then constrain both C/O and O/H by fitting the OH lines and the CO band head at the same time. Since we are focussing on evolutionary abundance changes in this paper, we made no attempt to derive an accurate oxygen abundance for these stars. However, we can clearly constrain the oxygen abundance to be close to a scaled solar value since the model presented in Fig. 4 obviously fits both features nicely with the same set of abundances. We estimate the uncertainty to be less than 0.1 dex. Keeping this small uncertainty in mind and assuming that the oxygen abundance is not changing along the giant branch of 47 Tuc, we derive a C/O ratio for our sample stars in the following.

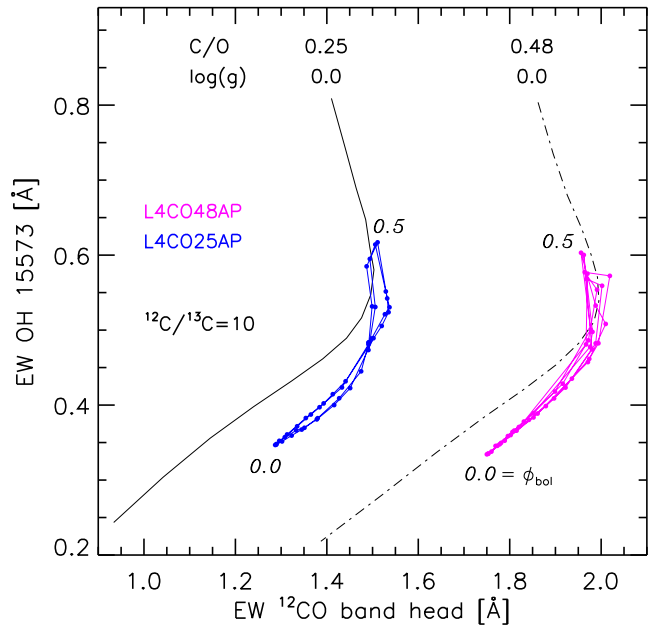


Fig. 7. Equivalent widths in $[\text{\AA}]$ of the OH line at 15573 \AA versus the strength of the ^{12}CO band head. Black lines mark temperature sequences for $\log g = 0.0$ and two different C/O ratios. The two coloured lines show the behaviour of the dynamic models L4C048AP and L4C025AP. Maximum and minimum phases are indicated ($\Phi_{\text{bol}} = 0.0$ and 0.5 , respectively). For all calculations a $^{12}\text{C}/^{13}\text{C}$ ratio of 10 was assumed.

For a given $\log g$ value we get a very clear separation according to the C/O ratio of 0.25 and 0.48. It is also obvious that the dynamical models – we use here L4C025AP and L4C048AP as representative examples – allow a clear distinction between two different C/O ratios as well. The $\log g$ value of 0.0 chosen here for the MARCS models brings the hydrostatic models closest to the dynamical ones. It is interesting to note that the variability during the pulsation cycle in the dynamical models produces effects that are rather similar to a sequence of hydrostatic models with fixed $\log g$ and different effective temperatures.

Dynamical models with C/O=0.25 show similar or even stronger ^{12}CO band heads than hydrostatic models with a $\log g$ value of 1.0 as shown in Fig. 8, where we added the 47 Tuc stars to the plot. Dynamical models with C/O=0.48 have been excluded from the plot since they are outside the range of the observed EWs. For illustrative purposes we have also included in Fig. 8 the range in EWs covered by the dynamical model L4C025CPM1, which shows NIR colours that are far too red.

The non-variable 47 Tuc stars all show similar values in Fig. 8 and are located close to the temperature sequence of the hydrostatic models with $\log g = 1.0$ and a C/O ratio of 0.25. On the same sequence, we find the mildly variable star V7 and the long-period variable V1. However, an inspection of the spectrum of the latter reveals very strong differences from a hydrostatic case, therefore the agreement has to be seen as a coincidence. All the other variables are found in the upper right-hand part of Fig. 8, clearly separated from the non-variable giants.

Figures 7 and 8 strongly suggest that the C/O ratio in the 47 Tuc stars is below 0.48. This is also expected from stellar evolution theory considering their low mass. We therefore decided to focus on the models with C/O=0.25 in the following, namely L4C025AP, L3C025AP, and L3C025BP.

² For the two strong OH lines next to the CO band head, the effect of abundance changes on the line strengths is fairly weak

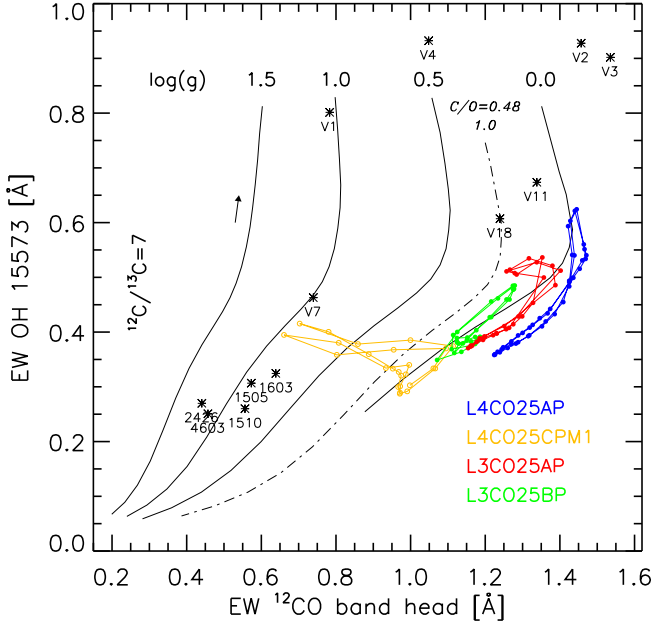


Fig. 8. Equivalent widths in [Å] of the OH line at 15573 Å versus the strength of the ^{12}CO band head. The 47 Tuc stars (Table 1) are marked with asterisks. Sequences of hydrostatic models (with varying T_{eff} but constant $\log g$) are shown as black lines, the corresponding $\log g$ values are labelled at the top of these lines. The small arrow indicates the trend of decreasing temperature. Coloured lines mark the location of selected dynamical models during the light cycles. For all models, the carbon isotopic ratio $^{12}\text{C}/^{13}\text{C}$ was set to 7. The C/O ratio is 0.25 if not stated otherwise.

For completeness we mention that in all cases a carbon isotopic ratio of 7 was used, but this parameter has only a weak effect on the ^{12}CO band-head strength. The other two OH features measured (see Table 2) show identical behaviour.

4.1.2. Constraining the $^{12}\text{C}/^{13}\text{C}$ ratios

In Fig. 9 we compare the strengths of the ^{12}CO and the ^{13}CO band heads. Hydrostatic temperature sequences are shown for three different $^{12}\text{C}/^{13}\text{C}$ ratios and various $\log g$ values. The three dynamical models selected in the previous step are plotted as well. As can be seen from Fig. 9, the mass-losing model L4C025CPM1 does not reproduce the observed strengths of the band heads either. To explore the effect of a varying carbon isotopic ratio on the synthetic spectra of the dynamical models, we calculated the corresponding values for $^{12}\text{C}/^{13}\text{C}$ ratios of 10 and 30 for model L4C025AP, for all the other dynamical models a value of 7 was used. The dynamical models cover an area in this diagram that starts at somewhat stronger ^{12}CO band heads than the hydrostatic models for a given depth of the ^{13}CO band head and ends in the same area as the low-temperature and low-surface gravity hydrostatic models.

All non-variable stars are found close to the hydrostatic temperature sequences. As in Fig. 8 a $\log g$ value close to 1.0 seems appropriate which agrees with the value estimated from the colour, brightness, and mass of these stars (Sect. 3.2). For most stars, an isotopic ratio of 7 provides a good fit. Two stars, Lee1510 and Lee1603, are fitted better by a slightly higher ratio. Similar to our comparison of the EWs of the OH line and the ^{12}CO band head (Fig. 8), V1 and V7 are found near the hydrostatic sequences as well. V2, V11, and V18 are close to the

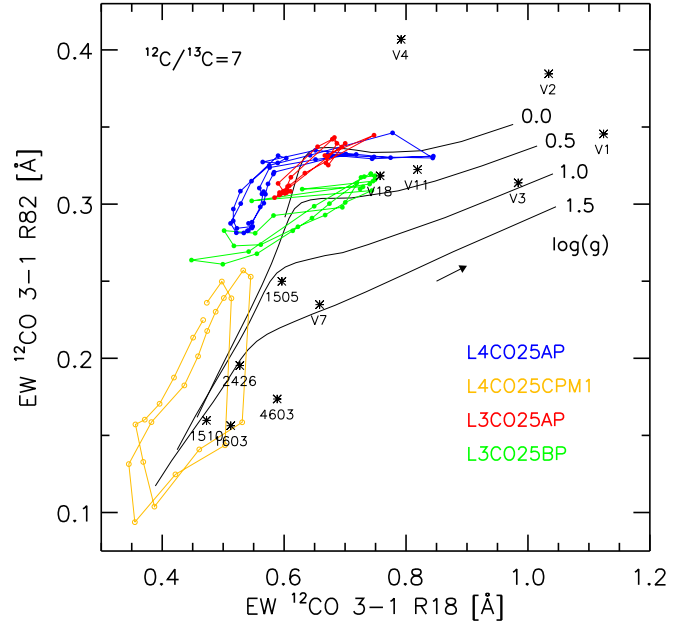


Fig. 10. Equivalent widths in [Å] of the high excitation CO 3-1 R82 line versus the low excitation CO 3-1 R18 line. Same symbols and line styles as in Fig. 8.

low-temperature end of the hydrostatic $\log g = 0$ sequence for $^{12}\text{C}/^{13}\text{C} = 10$. It is possible that V4 could be brought into agreement with a hydrostatic model with $^{12}\text{C}/^{13}\text{C} > 10$. We discuss this aspect below. The uncertainty in the band strengths is typically 0.04 Å. Therefore the measurement error has a very weak effect on the results. Finally, V3 is found separated from the other stars but within the range in EWs covered by the dynamical models.

4.1.3. Investigation of different line-forming regions

In Fig. 10 we compare two CO 3-1 lines of different excitation energies. In the extended atmospheres of red giants the R18 line and the R82 line will be formed at quite different atmospheric depths. The excitation energy of R18 is 2794.0743 cm^{-1} , while the excitation energy of R82 is $14826.3718\text{ cm}^{-1}$. This is, in particular, relevant for the variable stars where a study of the two lines permits comparison of atmospheric structure and inherent velocity fields with models. This approach has been applied to AGB stars in various papers in the past (e.g. Hinkle et al. 1982; Wallerstein 1985; Nowotny et al. 2005, 2010). All modelling results for this figure were calculated with a carbon isotopic ratio of 7 and C/O = 0.25. However, neither parameter has a significant effect on the results shown here.

Figure 10 is structured in a similar way to the previous ones. The dynamical models are now closer to the hydrostatic relations, suggesting that dynamical effects are not that prominent in these lines. For effective temperatures above 3600 K, the R82 line is obviously a good indicator for T_{eff} , while the dependency on $\log g$ is quite weak in this temperature regime. For lower temperatures this parameter can be derived using the low excitation R18 line. Lee 1505, Lee 1510, Lee 1603, and Lee 1505 behave as in all the other diagrams. Lee 4603 is somewhat offset, but the reason for this is not clear. The variables besides V7 are all found in the upper right-hand part of the diagram. V4 has a remarkably strong R82 line. Inspection of the line profile reveals a significant broadening due to line doubling.

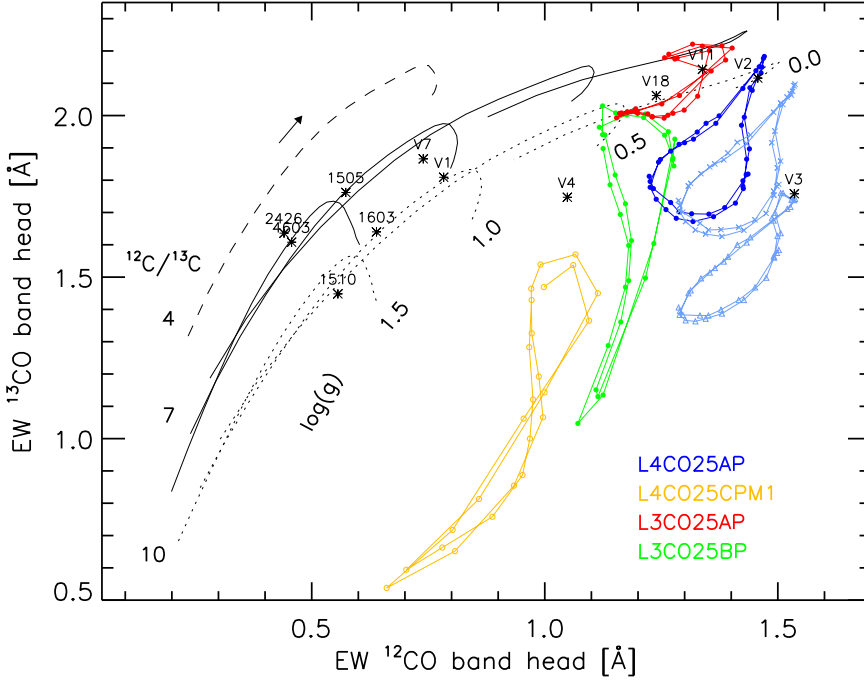


Fig. 9. Equivalent widths in \AA of the ^{13}CO band head versus the ^{12}CO band head. 47 Tuc stars are marked with asterisks. Black lines indicate effective temperature sequences of hydrostatic MARCS models for various constant $\log g$ values and three different values for the carbon isotopic ratio $^{12}\text{C}/^{13}\text{C}$ (as labelled). The temperature is decreasing in the direction of the small arrow. Coloured lines again show the location of the dynamical models with a carbon isotopic ratio of 7 assumed. In the case of L4CO25AP, we show also the results for differing $^{12}\text{C}/^{13}\text{C}$ ratios of 10 and 30 (light blue).

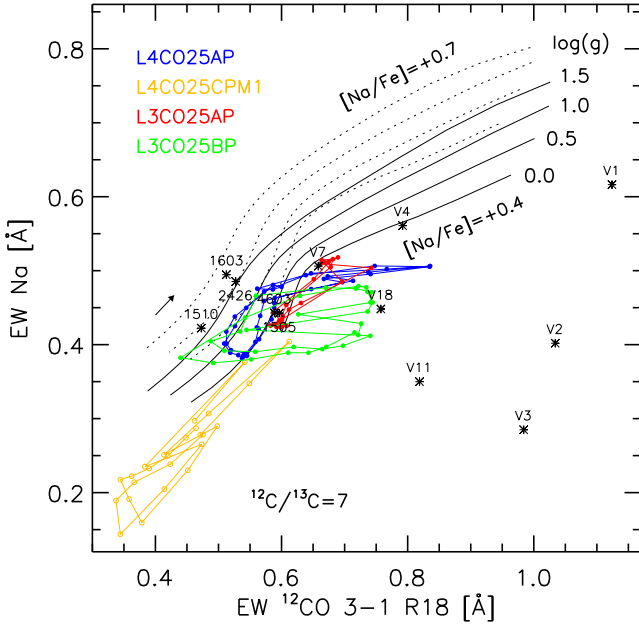


Fig. 11. Equivalent widths in \AA of the sodium line at 23383 \AA versus the EW of the ^{12}CO 3-1 R18 line. Same symbols and line styles as in Fig. 8. Hydrostatic models are plotted for $[\text{Na}/\text{Fe}]=+0.4$ and $+0.7$, dynamical models for $[\text{Na}/\text{Fe}]=+0.4$, respectively.

4.1.4. Sodium as an example for atomic lines

The 2.3383 μm sodium (Na) line, located within the spectral range covered by our K -band observation, was selected as representative of an atomic line. Its line profile has little contamination by other spectral lines (at least in the hydrostatic case). The EWs for this spectral line derived from observations, hydrostatic and dynamical models are plotted in Fig. 11 against the ^{12}CO 3-1 R18 line strengths. These two line strengths are related almost

linearly to each other making this result simpler than sodium line strengths against, for instance, the ^{13}CO band head strength. In either case, the derived conclusions are very similar.

Following published Na abundances we used an overabundance of Na relative to Fe in our model calculations. Cordero et al. (2014) report $[\text{Na}/\text{Fe}]$ values between 0.0 and 0.9 dex in 47 Tuc stars, with the majority of objects showing overabundances relative to iron between 0.2 and 0.9 dex. This agrees with earlier results by other authors (e.g. Carretta et al. 2013). Since the spectra of the non-variable giants suggest a clear enhancement of the sodium abundance in these stars, we decided to compute two series of hydrostatic model spectra, one with $[\text{Na}/\text{Fe}]=+0.4$ and one with $[\text{Na}/\text{Fe}]=+0.7$. The findings from Cordero et al. (2014) suggest quite a large scatter in the sodium overabundance from star to star, so that our usual assumption on the similarity of abundances in our variable and non-variable sample stars is not necessarily correct. The uncertainty in this case is also illustrated by the difference observed between our non-variable giants: Lee 1510, Lee 1603, and Lee 2426 are nicely fitted with $[\text{Na}/\text{Fe}]=+0.7$ (for $\log g = 1.0$), while for the other Lee stars a value slightly below $[\text{Na}/\text{Fe}]=+0.4$ seems to be more appropriate.

The variable stars V4 and V7 are found near the hydrostatic temperature sequence for $\log g = 0.0$ and $[\text{Na}/\text{Fe}]=+0.4$. The other variables all show a weaker sodium line, which would require $[\text{Na}/\text{Fe}]$ values around 0.0 (V18) or clearly subsolar (V1, V2, V3, V11). The results of Cordero et al. (2014) make such low values extremely unlikely. We therefore conclude that the Na line is weakened in these variables by dynamical effects. We calculated synthetic spectra for the four dynamical models also used in the previous comparisons with $[\text{Na}/\text{Fe}]=+0.4$. The increase in EW for $[\text{Na}/\text{Fe}]=+0.7$ can be estimated from the corresponding difference seen in the hydrostatic models.

An obvious difference in the behaviour of the dynamical models shown in Fig. 11 compared with those shown in Fig. 9 is that the loops are not as smooth in this diagram. We think this is due to the appearance of emission in the blue wing of the ^{12}CO

3-1 R18 line at some phases. The effect is also visible in Fig. 10. The Na line does not show similar emission in the model spectra. The models L3C025AP and L4C025AP, i.e. the ones with the smallest piston amplitude, are found very close to the hydrostatic series with $\log g = 0.0$ and $[\text{Na}/\text{Fe}] = +0.4$ throughout the whole pulsation cycle. Model L3C025BP with a slightly larger piston amplitude exhibits a rather horizontal change in the diagram over a large portion of the light cycle. In fact, the EW of the Na line hardly changes between $\Phi = 0.9$ and 0.4 , while the ^{12}CO 3-1 R18 line shows a sinusoidal variation with phase. As a result of this difference, this dynamical model cannot be approximated by a temperature sequence of hydrostatic models at constant surface gravity. Finally, model L4C025CPM1 is clearly offset from the hydrostatic ones towards low EW values. Weak line strengths, also compared to the other dynamical models, are also found for the ^{12}CO 3-1 R82 line and the ^{12}CO 3-1 R18 line as can be seen in Fig. 10. Emission components appearing in the line profiles as mentioned above could be one cause but since the Na line does not show obvious emission components in the dynamical models, it seems to be more appropriate to describe this as a line weakening, a well known phenomenon in LPVs (e.g. Crowe & Garrison 1988).

4.2. Variability of EW over a pulsation cycle

The high S/N single-epoch observations used in the previous section do not permit a direct evaluation of the variations with phase seen in the model spectra. We therefore made use of an additional time series of spectra for our 47 Tuc variables, which was obtained for an earlier project (Lebzelter et al. 2005). Owing to the lower resolution and the lower S/N, we decided to focus on a single line that seemed to be least affected by neighbouring features, namely the ^{12}CO 4-1 P27 line (cf. Fig. 6). The strongest variations in EW were found in V1, V2, and V3, the stars with the largest pulsation amplitudes. The results are plotted against pulsation phase in the left-hand panel of Fig. 12. This plot combines data from more than one light cycle, so that cycle-to-cycle variations have to be considered as a source of additional scatter. The other 47 Tuc variables investigated – V4, V11, and V18 – show variations with an amplitude of typically 0.1 \AA with a similar dependency on the pulsation phase, i.e. maximum line strength near light minimum ($\phi \approx 0.5$).

The same trend can be observed for the dynamical models, most clearly expressed in L4C025AP, which is also shown in Fig. 12. However, the amplitude of the dynamical model is somewhat less than what is observed in V1 to V3. Still, this variation corresponds to a substantial change in temperature when compared with the hydrostatic models. Such a comparison can be done with the help of the right-hand panel of Fig. 12. This supports the finding from Paper I that the dynamical model atmospheres can qualitatively reproduce the observed variations in line strength. Model L4C025CPM1, the model with the largest bolometric amplitude, gives the same amplitude for the change in EW.

5. Discussion

5.1. C/O and $^{12}\text{C}/^{13}\text{C}$ ratios of red giants in 47 Tuc

For the five non-variable cluster giants studied in this paper (the Lee stars), the hydrostatic models provide fits to the observed spectra sufficient to derive elemental abundances. As noted above, the metallicity was set to a fixed value taken from the literature.

We start our analysis by constraining the C/O ratio using the relations plotted in Fig. 8. In the following we make the assumption that the five giants will have similar abundances; i.e., the star-to-star scatter is small, although it is of course clearly visible in the figures presented in the previous section. We also assume that the $\log g$ value derived from independent measurements is adequate. A value of $\text{C/O} = 0.25$ seems to give a reasonably good fit for the observations. Within the uncertainties of the measurement, the calculated T_{eff} values of the Lee stars (Table 1) are consistent with the temperatures of the best-fitting models in Fig. 8. Even allowing an uncertainty of 0.5 in the value for the surface gravity, the error of the C/O ratio would be limited to 0.1. The measured subsolar C/O ratio is consistent with a reduction of carbon on the surface by the first dredge-up, as well as the oxygen overabundance and carbon underabundance in pre-RGB stars in 47 Tuc measured by Carretta et al. (2005).

Next we determine the $^{12}\text{C}/^{13}\text{C}$ ratio with the help of the quantities plotted in Fig. 9. The combination of the ^{12}CO and ^{13}CO band heads has the convenient property that a change in C/O shifts the relation between the two feature strengths along the path for a constant isotopic ratio; i.e., it has no effect on the determination of the latter quantity. The carbon isotopic ratio can therefore be determined with an accuracy of ± 1 (for the range given here). For Lee 1505, Lee 2426, and Lee 4603, we find a ratio of 7, and for Lee 1510 and Lee 1603 a ratio of 10. For dwarfs in this cluster, Carretta et al. (2005) find isotopic ratios clearly above 10, while their sample of subgiants shows $^{12}\text{C}/^{13}\text{C}$ values between 9 and 12. Attributing this reduction to first dredge up suggests that the main sequence value was lower than the solar isotopic ratio, a consequence of primordial pollution with CN burning products in the cluster. The values for the subgiants are only slightly higher than the values we found for our RGB stars. This is consistent with the finding of Shetrone (2003) that the isotopic ratio of carbon stays nearly constant above the RGB bump. However, the mild reduction we see is likely due to extra-mixing on the RGB (e.g. Nollett et al. 2003; Eggleton et al. 2008; Lederer et al. 2009, and references therein).

5.2. Abundance determination in LPVs

The low stellar masses of the 47 Tuc AGB stars mean we can safely assume that the surface abundance is not altered by third dredge up (e.g. Straniero et al. 2003). Combined with the small scatter of the abundances found for our five red giants, we expect to find abundances similar to the red giants for the AGB stars. This allows us to study the effect of the dynamics on the abundance determination.

We compare different observed spectroscopic features with results of hydrostatic models, identifying discrepancies and/or inconsistencies. The fundamental stellar parameters, i.e. mass, luminosity, and T_{eff} , derived for the LPVs in the 47 Tuc sample suggest $\log g$ values between -0.2 and 0.5 as appropriate. For each spectroscopic feature we explore how the feature strength compares with the prediction from the model.

We start with the OH 15573 line versus the ^{12}CO band head, used for determining C/O (Fig. 8). V1 and V7 are found close to a temperature sequence of hydrostatic models with $\log g = 1.0$; i.e., the ^{12}CO band head comes out too weak or the OH line is too strong to place them on a sequence corresponding to an appropriate $\log g$. Surface gravities derived from mass, colour, and luminosity, as done here, therefore indicate a C/O ratio of significantly less than 0.25 in both cases (to shift a temperature sequence with a given $\log g$ to the left in Fig. 8). This is, however, unrealistic, indicating that the lines are affected by dynamics. In

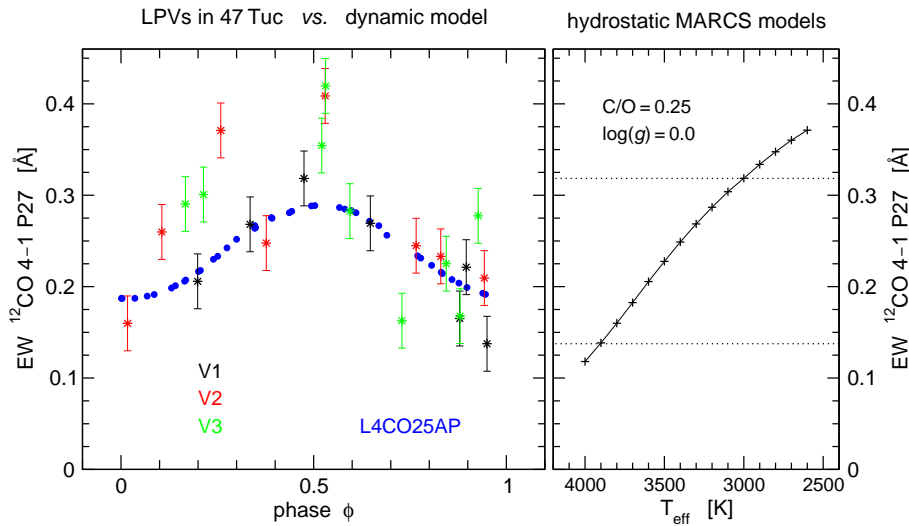


Fig. 12. *Left:* Variation in the equivalent widths in [Å] of the ^{12}CO 4-1 P27 line over the light cycle for the three 47 Tuc LPVs with the largest photometric amplitudes (V1, V2, V3, colour coded). Also shown is the corresponding variation with pulsation phase as derived for the dynamical model L4C025AP. *Right:* Line-strength variation of the same line for one T_{eff} -sequence of hydrostatic models with $\log g = 0.0$. The dotted lines mark the total range of equivalent widths measured for V1.

this context it is interesting to recall that the dynamical model L4C025CPM1 predicts a change over the pulsation cycle reaching from the area of hydrostatic models with $\log g = 0$ to those with $\log g = 1.0$. In this sense, a difference between the observed EW and the expected $\log g$ value might be reproducible by dynamical models.

V11 and V18 are located within the expected $\log g$ range, so a hydrostatic model would lead to a consistent C/O ratio of 0.25. For V2, V3, and V4 we measure very strong OH lines, most likely due to line doubling as outlined below. All three stars are found beyond the end of our model sequences. From the stellar parameters derived in Sect. 2, the $\log g$ value of V4 is expected to be closer to 0, so the star is somewhat offset to the left of the corresponding hydrostatic sequence. The CO band-head strength of V2 and V3 is consistent with the estimated surface gravities around $\log g = -0.2$ and a C/O ratio of 0.25 for these two stars. A C/O ratio of 0.48 (indicated in Fig. 8 by the dash-dotted line for $\log g = 1.0$) is only possible if the surface gravity of the two variables is significantly higher than expected. However, since the concept of determining stellar parameters for long-period variables has to be seen with caution, the C/O ratio determined in this way comes with some uncertainty. Nevertheless, we note the consistency of the findings with the assumption of a rather constant C/O for all objects on the upper giant branch of 47 Tuc.

It is interesting to compare this result with the pulsation phases at the time of observation. Since the light curves of V7, V11, and V18 are not regular enough to allow for determining a reliable pulsation phase, we restrict ourselves to V1, V2, V3, and V4. We found that V2 and V3 show line strength that is very comparable to a hydrostatic model of similar $\log g$. Their pulsation phases are 0.35 and 0.18, respectively. V1 and V4, which both show an offset, were observed at phases 0.9 and 0.8, respectively. The dynamical model L4C025CPM1 shows a similar offset at some phases. However, the model reaches the maximum offset near light minimum, i.e. phase 0.5. Up to this point we have focussed on the $\log g$ value in our comparison. However, we also have to take a closer look at the temperature, even though the concept of defining a T_{eff} value is questionable for the highly extended atmospheres of AGB variables. Still we immediately note that stars like V1, V2, V3, or V4 are found close to the low-temperature end of our hydrostatic sequences, corresponding to temperatures of 2600 K or even less. Observed NIR colours, however, suggest a significantly higher temperature at the time of the observations (see Table 1). The difference

of 900 K is also far more than what would be expected at any time during the light cycle. Furthermore, no spectra of the four stars were obtained near minimum light where we would expect the star to be reddest. Therefore, while the $\log g$ values seem to be consistent with the observed EWs, the temperature values we estimate from NIR photometry are not. The reason for this can be easily seen in the upper panel of Fig. 5. The OH line at 15573 Å we study here is clearly broadened in V2 by a second component; i.e., we see a case of beginning line doubling. This leads to an increased EW of the line.

In summary, for this feature we find that C/O ratios derived from the two-feature-strength plot presented in Fig. 8 under the assumption of a given $\log g$ value are either as expected or lower. Our observations suggest a dependency of this offset on phase. The feature strengths are inconsistent with an effective temperature derived under hydrostatic assumptions.

In the case of the comparison between the ^{12}CO and ^{13}CO band head (Fig. 9), V1 and V7 show similar behaviour to the previous two features studied; i.e., the measured EWs correspond to a $\log g$ value significantly higher than expected. We note the bending of the hydrostatic temperature sequences at the low-temperature end. V1 is indeed at the end of the $\log g = 1.0$ sequence for an isotopic ratio $^{12}\text{C}/^{13}\text{C}=7$, not on the $^{12}\text{C}/^{13}\text{C}=10$ sequence. Therefore, this is completely consistent with the findings from Fig. 8 regarding the $\log g$ value. The same is true for V4, which is again found somewhat above the low-temperature end of the $\log g = 0.5$, $^{12}\text{C}/^{13}\text{C}=7$ sequence. V2, V11, and V18 give band strengths similar to the predictions of a hydrostatic model with $\log g = 0.0$. The only variable with a different behaviour is V3, which probably has too weak a ^{13}CO band head. The most trivial explanation that the star has a higher carbon isotopic ratio would require either a dredge up of ^{12}C on the AGB, which is very unlikely in these stars and which would also manifest itself in a different C/O ratio, or the absence of extra-mixing on the first giant branch, which poses the question why this single star has undergone a different evolution or had a different primordial isotopic ratio. While possible, we find also a deviating behaviour of V3 in another spectral feature as discussed below. For the comparison of the two band heads we end up with the same and consistent conclusion as for the comparison of the ^{12}CO band head and the OH line. Again, an effective temperature consistent with the measured EWs is inconsistent with the colours of these stars.

Table 5. Qualitative description of the line shapes of the ^{12}CO 3-1 lines R18 and R82.

Object-ID	R18	R82
V1	doubled, red weak	slightly broadened
V2	doubled, similar strength	broadened
V3	doubled, blue weak	slightly broadened
V4	single, broadened	broadened
V7	single	single
V11	single, slightly broadened	slightly broadened
V18	single	single

5.3. Atmospheric structure and dynamics of LPVs

Comparison of the EWs of the two ^{12}CO 3-1 lines we plotted in Fig. 10 provides insight into the stellar atmospheric structure since both lines are affected by abundance changes in a very similar way. In particular, the differential velocity fields in the stellar atmosphere resulting from the pulsation significantly change the line profile of these moderate excitation CO lines as illustrated by the line doubling visible in the lower panel of Fig. 5 (cf. Hinkle et al. 1982). Inspection of these two lines in the K -band spectra of our seven variables reveals a variety of line profiles which we summarize in Table 5.

We first discuss the stars showing neither line doubling nor strong line broadening, i.e. V7, V11, and V18. V7, a star behaving very consistently in all other features discussed, shows a value that places it close to the hydrostatic $\log g = 1.5$ sequence; i.e., for our hydrostatic approach either its R82 line is too weak or both lines are too weak. Considering its typical location along the temperature sequence in the other diagrams, the latter case is more likely. This finding is very interesting since it indicates that even stars that are thought to be quasi-hydrostatic owing to their small pulsation amplitude still can exhibit clear signatures of a non-hydrostatic atmospheric structure. In this context we also have to note the slight broadening of these lines in V11 compared to a hydrostatic case. However, the line strengths in the spectrum of V11, and also in V18, are not outstanding and are consistent with the results from the other features where these stars show no strong deviation from the hydrostatic models.

In the spectral features discussed above the occurrence of line doubling led to a location in our two-feature diagrams consistent with our derived $\log g$ value but inconsistent with the colour temperature. In the case of the two CO lines, this is true for V2, but not for V3 and V4, both deviating strongly from the hydrostatic $\log g = 0$ sequence. At this point, the limitations of fitting dynamical stars with hydrostatic models are clearly illustrated. However, none of our dynamical models studied here reaches the line strengths observed in the large amplitude 47 Tuc variables. For completeness we note that V1, which shows indications of line doubling in both CO lines, behaves consistently with what we found for the other spectral features.

Since the primordial scatter of the Na abundance is quite large in 47 Tuc, the Na line in our spectra is only of limited use in estimating the dynamical effects on the abundance determination. However, the strong offset of V1, V2, and V3 from the other giants in Fig. 11 suggests that the Na line is weaker in the dynamical case than in hydrostatic models of similar stellar parameters. The behaviour of the dynamical models suggest that there might be phases where the sodium line strengths approach the hydrostatic case, but to check this spectroscopic time series

covering a whole light cycle for at least one of the large amplitude variables would be needed.

5.4. Behaviour of the dynamical models

While the limited set of dynamical models used in this study led to some qualitative improvements compared to hydrostatic models, it did not provide satisfactory quantitative fits for all investigated features of the long-period variables of 47 Tuc. However, the four different sets of parameters for the models analysed in detail in Sect. 4.1 permit a study of the effects of these parameters on the EWs of the synthetic spectral features. We noted above that for some spectral features temporal variations of the dynamical models closely resemble a hydrostatic temperature sequence at constant $\log g$, while in other features they strongly deviate from the hydrostatic models. The deviation from the hydrostatic case is more obvious for the band heads studied – see in particular Figure 9 – than for individual atomic or molecular lines. The spectra of V3 and V4 support the possibility that such deviations in the ^{13}CO band head strength from the hydrostatic case occur in real LPVs.

A main result of Paper I was the discovery of an asymmetry in the variation of the feature strengths between the rising and the descending branch of the light curve. As a result, the models – and also observed miras – produce a loop in a diagram showing feature strength vs. colour. In the present paper we show that these loops are found also in diagrams relating two feature strengths with one another. The loops are reminiscent of loops in colour-colour diagrams due to phase-shifted variations of molecular features originating in different layers (Bladh et al. 2013). Although one can recognize some differences in the location and extension of such loops our limited set of models does not permit the identification of systematic dependencies with any model parameter.

In dynamical models abundance differences not only lead to an overall shift of the curves (as found for the hydrostatic models) describing EW change over a pulsation cycle but can also affect the shape of that loop. This is clearly seen for model L4C025AP in Fig. 9 for curves of carbon isotopic ratios 7 (dark blue), 10, and 30 (light blue). The shape of the loop changes for an isotopic ratio of 30 producing a double loop structure. Since all these three calculations are based on the very same atmospheric structure, this demonstrates the strong effect of shifting the line forming region in geometrical distance depending on the adopted isotopic ratio in the case of dynamical atmospheres. A similar change is seen for the C/O ratio in Fig. 8.

6. Conclusions

In this paper we derived abundances for a small sample of red, non-variable giants in the globular cluster 47 Tuc. Assuming no abundance changes due to third dredge up or other mixing processes in the cluster’s low mass AGB stars we tested various options for deriving elemental abundances for long period variables. Our high-resolution spectra of the AGB variables in 47 Tuc reveal that the objects with the largest variability amplitudes show effects on the line profiles due to atmospheric velocity fields that cannot be reproduced by hydrostatic models. As illustrated in Fig. 5, dynamical model atmospheres can in principle produce similar line components (see also Nowotny et al. 2005). However, none of the nine configurations of the dynamical models tested here (Table 4) gave a good fit to the entire observed high-resolution spectra. Nevertheless, the dynamical

model fits the observed spectrum of the large-amplitude variable V2 much better than any hydrostatic model, thereby indicating the potential of dynamical model analysis of high-resolution LPV spectra.

In our analysis, we concentrated on comparing observed and modeled equivalent widths of selected spectral features. While the range of values covered by hydrostatic and dynamical models shows some overlap with the observed values, neither hydrostatic nor dynamical models were able to provide a consistent fit for any of the four most variable stars, V1, V2, V3, and V4. Some success for a fit with a single hydrostatic model could be achieved for the mildly pulsating stars V11 and V18, although – as for the other variables – the corresponding temperature of a hydrostatic model with the same equivalent widths and the same $\log g$ value is much lower than what would be expected from the stars' colours. The fitting of V18 by a single hydrostatic model is remarkable since the star shows significant dust mass loss, and therefore one would expect an atmospheric structure that shows clear signs of stellar pulsation³. For the third small amplitude LPV in our sample, V7, a model producing good fits was not found.

We can compare our findings with the work by McSaveney et al. (2007), who made a similar attempt to derive element abundances from NIR spectra of some LMC AGB stars. They identify the time around visual light minimum as the best one for this task, while spectra obtained close to light maximum could not be fitted with synthetic spectra. In the intermediate mass stars studied in their paper, the shock enters the atmosphere around phase 0.7 to 0.8 and leaves it again near phase 0.4. The spectroscopic time series of the 47 Tuc variables V1 to V3 presented in Lebzelter et al. (2005) suggest the presence of line doubling, hence of a shock in the atmosphere, between phases 0.75 and 0.2, i.e. very similar to the intermediate mass stars. Unfortunately, we do not have any Phoenix observations obtained near light minimum, therefore we cannot directly test the finding of McSaveney et al. (2007) that the minimum is the best phase to measure element abundances. Our coverage of a complete pulsation cycle in the ^{12}CO 4-1 P27 line (Figure 12) does not favour a particular pulsation phase in terms of a better model fit. The range of measured equivalent widths of that line in the 47 Tuc variables agrees with the range covered by the hydrostatic models for $\log g = 0$, although it again requires that quite low temperatures are reached by the variables, temperatures too low to have a counterpart in the near-infrared colours.

The dynamical models tested here did not properly reproduce the equivalent widths for the 47 Tuc variables. One difficulty lies in the selection of the parameters of the starting model based on observational quantities. We showed that agreement in luminosity, colour indices, and metallicity, and an approximate agreement in the K amplitude is not sufficient to obtain a model that satisfactorily fits the strengths of observed spectral features. It is not clear whether this indicates a problem in the model structure or the need to improve the model selection by including further stellar parameters. An obvious problem is a realistic description of the mass loss in these stars. Some of the 47 Tuc stars clearly show a dusty mass loss, but none of the three dynamical models that develop winds produces realistic spectra. The two models where the outflows are driven by true absorption on dust

grains do not reproduce the observed near-infrared colours. The remaining model, if assuming pure scattering on dust grains as a driving force, shows problematic emission features. It is reasonable to assume that also under the conditions in the 47 Tuc AGB stars dust formation in the stellar atmosphere will affect the atmospheric structure and extension. This, again, would influence the line strengths in the spectra. To tackle this problem, a better understanding of mass loss and dust formation in these low-luminosity and low-metallicity AGB stars is clearly necessary.

Keeping in mind the variety we see in the observations and the uncertainties in the dynamic models regarding the fundamental parameters and the wind mechanism, it is clear that the study presented in this paper and in Paper I is a limited first effort on the highly complex topic of determining element abundances and isotopic ratios for large-amplitude variable stars. Hydrostatic models of low $\log g$ and an effective temperature lower than what is consistent with photometry can be useful for extracting the stellar composition from the high-resolution spectra of AGB variables, but the results come with considerable uncertainties that are far beyond observational errors. In general, selecting stars with smaller light amplitudes eases the fitting process. However, our study also shows that even mildly pulsating stars can have spectral line strengths that cannot consistently be fit with hydrostatic models.

Abundance offsets between values derived from hydrostatic models and the corresponding variable star observations need to be validated by further investigations. The path followed here – using AGB variables for which the abundances can be predicted from other, non-variable sources – seems to be a good choice for this validation process. But also for the next step, deriving abundances directly from AGB variables, ensembles of such objects in stellar clusters could be the preferred target since the expected similarity of the abundance pattern can be used to average out the dynamical effects acting in individual stars.

Acknowledgements. This work has been supported by the Austrian Science Fund (P23737-N16, P21988-N16) and the Swedish Research Council. The National Optical Astronomy Observatory is operated by the Association of Universities for Research in Astronomy, Inc. under cooperative agreement with the National Science Foundation. This work is based in part on observations obtained at the Gemini Observatory, which is operated by the Association of Universities for Research in Astronomy, Inc., under a cooperative agreement with the NSF on behalf of the Gemini partnership: the National Science Foundation (United States), the National Research Council (Canada), CONICYT (Chile), the Australian Research Council (Australia), Ministério da Ciência, Tecnologia e Inovação (Brazil), and Ministerio de Ciencia, Tecnología e Innovación Productiva (Argentina). The authors wish to thank Dick Joyce for doing most of the data reduction for the Mount Stromlo spectra. Oscar Straniero provided fruitful discussion on the atmospheric mixing. This publication used data products from the Two Micron All Sky Survey, which is a joint project of the University of Massachusetts and the Infrared Processing and Analysis Center/California Institute of Technology, funded by the National Aeronautics and Space Administration and the National Science Foundation. This research also made use of the SIMBAD database, operated at the CDS in Strasbourg, France, and NASA's Astrophysics Data System Bibliographic Services.

References

- Anders, E. & Grevesse, N. 1989, *Geochim. Cosmochim. Acta*, 53, 197
- Aringer, B., Girardi, L., Nowotny, W., Marigo, P., & Lederer, M. T. 2009, *A&A*, 503, 913
- Bessell, M. S. & Brett, J. M. 1988, *PASP*, 100, 1134
- Bessell, M. S., Scholz, M., & Wood, P. R. 1996, *A&A*, 307, 481
- Bladh, S. & Höfner, S. 2012, *A&A*, 546, A76
- Bladh, S., Höfner, S., Nowotny, W., Aringer, B., & Eriksson, K. 2013, *A&A*, 553, A20
- Carretta, E., Gratton, R. G., Bragaglia, A., D'Orazi, V., & Lucatello, S. 2013, *A&A*, 550, A34

³ We note that the dust signatures of this star could be the result of a higher mass loss rate in the past, so the current mass loss rate could be lower. See the discussion on the evolutionary status of V18 in Lebzelter et al. (2006).

- Carretta, E., Gratton, R. G., Lucatello, S., Bragaglia, A., & Bonifacio, P. 2005, A&A, 433, 597
- Cordero, M. J., Pilachowski, C. A., Johnson, C. I., et al. 2014, ApJ, 780, 94
- Crowe, R. A. & Garrison, R. F. 1988, ApJS, 66, 69
- Eggleton, P. P., Dearborn, D. S. P., & Lattanzio, J. C. 2008, ApJ, 677, 581
- Eriksson, K., Nowotny, W., Höfner, S., Aringer, B., & Wachter, A. 2014, ArXiv e-prints
- Feast, M. W. 1996, MNRAS, 278, 11
- Frogel, J. A. 1983, ApJ, 272, 167
- Frogel, J. A. & Elias, J. H. 1988, ApJ, 324, 823
- Frogel, J. A., Persson, S. E., & Cohen, J. G. 1981, ApJ, 246, 842
- Glass, I. S. & Feast, M. W. 1973, MNRAS, 163, 245
- Grevesse, N. & Sauval, A. J. 1994, in Lecture Notes in Physics, Berlin Springer Verlag, Vol. 428, IAU Colloq. 146: Molecules in the Stellar Environment, ed. U. G. Jørgensen, 196
- Hinkle, K., Wallace, L., & Livingston, W. C. 1995, Infrared atlas of the Arcturus spectrum, 0.9-5.3 microns
- Hinkle, K. H., Blum, R. D., Joyce, R. R., et al. 2003, in Society of Photo-Optical Instrumentation Engineers (SPIE) Conference Series, Vol. 4834, Discoveries and Research Prospects from 6- to 10-Meter-Class Telescopes II, ed. P. Guhathakurta, 353–363
- Hinkle, K. H., Hall, D. N. B., & Ridgway, S. T. 1982, ApJ, 252, 697
- Höfner, S. 2008, A&A, 491, L1
- Höfner, S., Gautschi-Loidl, R., Aringer, B., & Jørgensen, U. G. 2003, A&A, 399, 589
- Lebzelter, T., Nowotny, W., Höfner, S., et al. 2010, A&A, 517, A6 (Paper I)
- Lebzelter, T., Posch, T., Hinkle, K., Wood, P. R., & Bouwman, J. 2006, ApJ, 653, L145
- Lebzelter, T. & Wood, P. R. 2005, A&A, 441, 1117
- Lebzelter, T., Wood, P. R., Hinkle, K. H., Joyce, R. R., & Fekel, F. C. 2005, A&A, 432, 207
- Lederer, M. T., Lebzelter, T., Cristallo, S., et al. 2009, A&A, 502, 913
- Lee, S.-W. 1977, A&AS, 27, 381
- McDonald, I., Boyer, M. L., van Loon, J. T., et al. 2011, ApJS, 193, 23
- McDonald, I. & van Loon, J. T. 2007, A&A, 476, 1261
- McSaveney, J. A., Wood, P. R., Scholz, M., Lattanzio, J. C., & Hinkle, K. H. 2007, MNRAS, 378, 1089
- Menzies, J. W. & Whitelock, P. A. 1985, MNRAS, 212, 783
- Nollett, K. M., Busso, M., & Wasserburg, G. J. 2003, ApJ, 582, 1036
- Nowotny, W., Aringer, B., Höfner, S., & Eriksson, K. 2013, A&A, 552, A20
- Nowotny, W., Aringer, B., Höfner, S., Gautschi-Loidl, R., & Windsteig, W. 2005, A&A, 437, 273
- Nowotny, W., Höfner, S., & Aringer, B. 2010, A&A, 514, A35
- Origlia, L., Scaltriti, F., Anderlucci, E., Ferraro, F. R., & Fusi Pecci, F. 1997, MNRAS, 292, 753
- Ramdani, A. & Jorissen, A. 2001, A&A, 372, 85
- Salaris, M., Held, E. V., Ortolani, S., Gullieuszik, M., & Momany, Y. 2007, A&A, 476, 243
- Scholz, M. 1992, A&A, 253, 203
- Shetrone, M. D. 2003, ApJ, 585, L45
- Straniero, O., Domínguez, I., Cristallo, S., & Gallino, R. 2003, PASA, 20, 389
- Wallerstein, G. 1985, PASP, 97, 994
- Worthey, G. & Lee, H.-c. 2011, ApJS, 193, 1